

# APPROXIMATE INFERENCE FOR CONSTRUCTING ASTRONOMICAL CATALOGS FROM IMAGES

BY JEFFREY REGIER<sup>1</sup>, ANDREW C. MILLER<sup>2</sup>, DAVID SCHLEGEL<sup>5</sup>,  
RYAN P. ADAMS<sup>3,4</sup>, JON D. MCAULIFFE<sup>1</sup>, AND PRABHAT<sup>5</sup>,

*University of California, Berkeley*<sup>1</sup>, *Harvard University*<sup>2</sup>, *Google Brain*<sup>3</sup>,  
*Princeton University*<sup>4</sup>, and *Lawrence Berkeley National Laboratory*<sup>5</sup>

We present a new, fully generative model for constructing astronomical catalogs from optical telescope image sets. Each pixel intensity is treated as a Poisson random variable with a rate parameter that depends on the latent properties of stars and galaxies. These latent properties are themselves random, with scientific prior distributions constructed from large ancillary datasets. We compare two procedures for posterior inference: Markov chain Monte Carlo (MCMC) and variational inference (VI). MCMC excels at quantifying uncertainty while VI is 1000× faster. Both procedures outperform the current state-of-the-art method for measuring celestial bodies' colors, shapes, and morphologies. On a supercomputer, the VI procedure efficiently uses 665,000 CPU cores (1.3 million hardware threads) to construct an astronomical catalog from 50 terabytes of images.

---

*MSC 2010 subject classifications:* Primary 62P35; secondary 85A35

*Keywords and phrases:* astronomy, graphical model, MCMC, variational inference, high performance computing

**1. Introduction.** Astronomical surveys are the primary source of information about the universe beyond our solar system. They are essential for addressing key open questions in astronomy and cosmology about topics such as the life cycles of stars and galaxies, the nature of dark energy, and the origin and evolution of the universe.

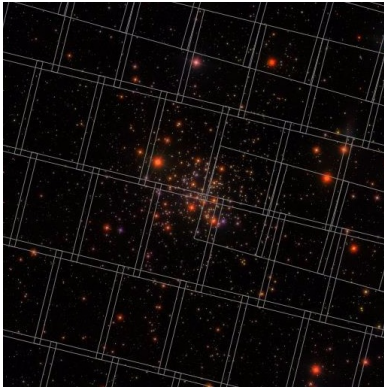


Fig 1: Sloan Digital Sky Survey (SDSS) data highlighting image boundaries. Some images overlap substantially. Some light sources appear in multiple images that do not overlap.

The principal products of astronomical imaging surveys are catalogs of light sources, such as stars and galaxies. These catalogs are generated by identifying light sources in survey images (e.g., Figure 1) and characterizing each according to physical parameters such as brightness, color, and morphology. Astronomical catalogs are the starting point for many scientific analyses, such as modeling groups of similar light sources or characterizing the spatial distribution of galaxies. For these “population-level” analyses, accurate quantification of uncertainty in parameters’ point estimates is as important as the accuracy of the point estimates themselves. Catalogs also inform the design of follow-on surveys using more advanced or specialized instrumentation. For example, catalogs are the basis for deciding what galaxies to observe with a spectrograph during scarce viewing time. With accurate uncertainty quantification, “portfolios” of galaxies can be selected to balance risk and expected reward.

Bayesian statistical inference is common throughout astronomy, e.g., for modeling stars’ spectra (von Hippel et al. 2006), for cosmology (Feroz et al. 2009), and for estimating supernova emissions (Mandel et al. 2011). Bayesian inference is also appealing as a way to reason about an astronomical catalog from intrinsically noisy data. Not only is prior information plentiful (Loredo

2013), but it also facilitates the construction of hierarchical models that can share structure and improve estimates across many light sources. An astronomical catalog’s entries may be modeled as unobserved random variables. Each pixel’s intensity—an observed random variable—is well modeled by a Poisson distribution with a rate parameter unique to the pixel. The posterior distribution induced over the unobserved physical properties of the light sources encapsulates knowledge about the catalog’s entries, combining prior knowledge of astrophysics with survey imaging data in a statistically efficient manner.

Up to now, most catalog-construction approaches have been based on computationally efficient heuristics rather than principled statistical methods (Lupton et al. 2005, Bertin & Arnouts 1996). The lack of statistical rigor may be due to the scale of the problem: modern astronomical surveys collect tens of terabytes of image data. Though computers are getting faster, the size of astronomical image sets is growing faster still. The upcoming Large Synoptic Survey Telescope (LSST) will collect 15 terabytes nightly—hundreds of petabytes in total (LSST 2017). Even basic management of these data requires substantial engineering effort. Catalog construction is also challenging because of the collective nature of the task: a light source’s properties cannot be accurately determined until any overlapping light sources’ properties are also known.

Heuristic approaches to catalog construction have a number of drawbacks: 1) they do not make optimal use of prior information because it is unclear how to “weight” it in relation to new information; 2) they do not effectively combine knowledge from multiple image surveys, or even from multiple overlapping images from the same survey; and 3) they do not quantify uncertainty of their estimates. While they may flag some estimates as particularly unreliable, calibrated uncertainties follow only from a statistical model. Without modeling the arrival of photons as a Poisson process, for example, there is little basis for reasoning about uncertainty in the underlying brightness of light sources.

Bayesian posterior inference is NP-hard for most probabilistic models of interest (Bishop 2006). Approximate Bayesian inference is an area of active research. Markov chain Monte Carlo (MCMC) is the most common approach. Two recent studies demonstrate that Bayesian modeling is the gold standard for astronomical inference, while casting doubt on whether MCMC is viable for constructing a whole astronomical catalog. Brewer et al. (2013) use a single 10,000-pixel image as the dataset for an MCMC procedure. Obtaining samples from the posterior distribution takes one day using a modern multi-core computer. Portillo et al. (2017) run twelve Intel Xeon cores for

an entire day to yield useful results on a similar dataset. The Sloan Digital Sky Survey—a modern astronomical survey—contains over a billion times as many pixels as these test images.

Before our work, Tractor (Lang & Hogg 2015) was the only program for Bayesian posterior inference that had been applied to a complete modern astronomical imaging survey. Tractor relies on the Laplace approximation: the posterior is approximated by a multivariate Gaussian distribution centered at the mode, having a covariance matrix equal to the negative Hessian of the log likelihood function at that mode. This type of approximation is not suitable for either categorical random variables or random variables with multi-modal posteriors—no Gaussian distribution approximates them well. Additionally, because Laplace approximation centers the Gaussian at the mode of the target rather than the mean, the solution depends on the parameterization of the problem (Bishop 2006).

Variational inference (VI) is an alternative to MCMC and the Laplace approximation. Like the latter, it uses numerical optimization, not sampling, to find a distribution that approximates the posterior (Blei et al. 2017). In practice, the resulting optimization problem is often orders of magnitude faster to solve compared to MCMC approaches. It can be simpler, too. Whereas MCMC transition operators must satisfy strict constraints for validity, the variational optimization problem can in principle be solved using any off-the-shelf technique. Scaling VI to large datasets is nonetheless challenging. To our knowledge, the dataset to which we apply VI is the largest ever, by at least one order of magnitude.

The remainder of this article assesses the potential for MCMC and VI to infer astronomical catalogs. Section 2 presents a novel probabilistic model for astronomical images. The model is designed primarily to reflect scientific knowledge; facilitating inference is secondary. Section 3 and Section 4 present inference procedures based on MCMC and VI, respectively. The MCMC procedure combines annealed importance sampling and slice sampling. The VI procedures break with VI tradition by optimizing based on explicitly computed gradients and Hessians rather than closed-form coordinate ascent updates. Section 5 presents experimental results for both inference procedures, applied to both synthetic and real astronomical images. MCMC better quantifies uncertainty, but VI is much faster. Section 6 describes scaling VI to the entire Sloan Digital Sky Survey (SDSS) using a supercomputer. Section 7 draws conclusions about each inference procedure. We consider not just the runtime and accuracy, but also our experiences deriving the algorithms, implementing them, and maintaining code for each inference technique.

**2. Statistical model.** Stars and galaxies radiate photons. An astronomical image records photons—each originating from a particular celestial body or from background atmospheric noise—that pass through a telescope’s lens during an exposure. Multiple light sources usually contribute photons to a single image, and sometimes even to a single pixel of an image.

Section 2.1 describes our model of light sources. Quantities of interest, such as location, color, and brightness, are random variables. Section 2.2 describes a generative model of astronomical images: the distribution of each pixel’s value—an observed random variable—depends on the latent variables that we aim to infer. Pixel intensities are conditionally independent given these latent random variables.

Figure 2 presents our statistical model as a graphical model. Table 1 lists the model’s structural constants. Table 2 lists the model’s random variables. Table 3 lists the model’s parameters.

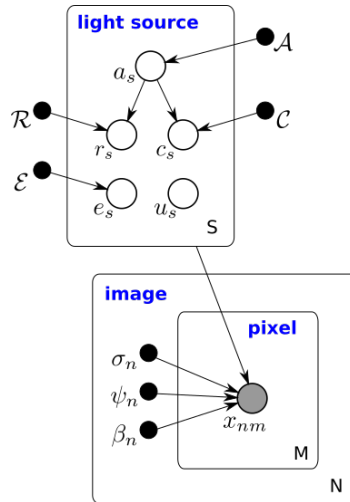


Fig 2: The proposed graphical model. The shaded vertex represents observed random variables. Empty vertices represent latent random variables. Black dots represent constants, set before inference takes places. Edges signify conditional dependencies. Rectangles (“plates”) represent independent replication. Tables 1, 2 and 3 summarize the variables.

2.1. *Light sources.* An astronomical catalog is a table with one row for each light source and one column for each quantity to estimate. The number of light sources,  $S$ , is a constant determined by an algorithmic preprocessing routine. Modeling  $S$  as random would be interesting extension to our model.

name	brief description	SDSS value
B	number of filter bands	5
E	number of PSF “eigenimages”	4
F	number of knots per PSF eigenimage	$51 \times 51$
H	number of rows of pixels per image	2048
I	number of source types (i.e., star, galaxy)	2
J	number of components in the color prior mixture	8
K	number of components in the galaxy mixture model	8
L	number of parameters in a WCS header	16
M	number of pixels per image	$H \times W$
N	number of images	4,690,230
Q	number of knots for the sky background model	$192 \times 256$
S	number of light sources	469,053,874
W	number of columns of pixels per image	1361

Table 1: Structural constants in our model

name	brief description	units	domain
$a_s$	galaxy / star indicator	unitless	$\{0, 1\}$
$c_s$	colors	magnitude	$\mathbb{R}^{B-1}$
$e_s^{angle}$	angle of galaxy’s major axis	degrees	$[0, 180)$
$e_s^{radius}$	galaxy’s half-light radius	arcseconds	$(0, \infty)$
$e_s^{profile}$	galaxy’s profile mixing weight	unitless	$[0, 1]$
$e_s^{axis}$	galaxy’s minor-major axis ratio	unitless	$(0, 1)$
$r_s$	reference-band brightness	nanomaggies	$[0, \infty)$
$u_s$	position (right ascension, declination)	degrees	$[0, 360) \times [-90, 90]$
$x_{nm}$	pixel intensity (observed)	photon count	$\{0, 1, 2, \dots\}$

Table 2: Random variables in our model

name	brief description	domain
$\mathcal{A}$	prior probability a light source is a star	$[0, 1]$
$\mathcal{C}^{weight}$	color prior mixture weights	$\mathbb{R}^{I \times J}$
$\mathcal{C}^{mean}$	color prior mixture component means	$\mathbb{R}^{I \times J \times (B-1)}$
$\mathcal{C}^{cov}$	color prior mixture component covariance matrices	$\mathbb{R}^{I \times J \times (B-1) \times (B-1)}$
$\mathcal{E}^{radius}$	galaxy half-light radius prior parameters	$\mathbb{R}^2$
$\mathcal{E}^{profile}$	galaxy profile prior parameters	$\mathbb{R}^2$
$\mathcal{E}^{axis}$	galaxy axis ratio prior parameters	$\mathbb{R}^2$
$\mathcal{R}$	reference-band brightness prior parameters	$\mathbb{R}^{I \times 2}$
$\sigma_n$	sky background model	$\mathbb{R}^Q$
$\psi_n^{calib}$	expected number of photons per nanomaggy	$\mathbb{R}^H$
$\psi_n^{wcs}$	image alignment	$\mathbb{R}^L$
$\psi_n^{weight}$	point spread function loadings	$\mathbb{R}^E$
$\psi_n^{image}$	point spread function principal components	$\mathbb{R}^{E \times F}$
$\beta_n$	filter band	$\{1, 2, \dots, B\}$

Table 3: Parameters in our model

All entries in the “table” are random, though the table’s dimensions are fixed following preprocessing.

Light sources in our model are either stars or galaxies, as are the vast majority of light sources in the universe. Exceptions include quasars and supernovae. Asteroids, planets, airplanes, and other satellites also occasionally appear in astronomical images. For light source  $s = 1, \dots, S$ , the latent random variable

$$(1) \quad a_s \sim \text{Bernoulli}(\mathcal{A})$$

indicates whether it is a star ( $a_s = 1$ ) or a galaxy ( $a_s = 0$ ). Here  $\mathcal{A}$  is a global prior representing the marginal probability that a given light source is a galaxy.

We set all prior parameters, including  $\mathcal{A}$ , based on pre-existing astronomical catalogs. Their values remain fixed during inference. Alternatively, these parameters could be set during inference through empirical Bayes. The latter approach makes inference more tedious to implement in software, particularly in a distributed setting, because all light sources are then coupled together by their shared prior. Fortunately, pre-existing catalogs are a good representation of our prior knowledge.

The latent random two-vector

$$(2) \quad u_s \sim \text{Uniform}([0, 360] \times [-90, 90])$$

denotes the position of light source  $s$  in the units of the World Coordinate System (Greisen & Calabretta 2002). Figure 9 illustrates this system of coordinates. The first coordinate is right ascension and the second coordinate is declination. Both are measured in degrees. Treating light sources as uniformly distributed is a simplification—some regions of the sky are known a priori to have more light sources than others, e.g., the galactic plane. However, significant variation in light source density only occurs over a much larger scale than the uncertainty of our measurements—whole degrees rather than a fractions of an arcsecond (1/3600 degree). Additionally, it is a simplification to model light sources as positioned independently of each other: gravity can cause some clustering among light sources. This effect is minor, however, in the context of the quantities we estimate.

2.1.1. *Overall brightness.* The overall brightness of light source  $s$  may be quantified as its expected total radiation reaching a unit area of Earth’s surface, directly facing  $s$ , per unit of time. Alternatively, we can quantify brightness as the proportion of this radiation (per square meter, per second) that passes through each filter in a standardized filter set (Figure 8). Such a set

is called a photometric system. These standardized filters are approximately band-pass: each allows most of the energy in a certain band of wavelengths through, while blocking most of the energy outside the band. The physical filters attached to a telescope lens closely match the standardized filters of some photometric system.

In our model, we take the photometric-system approach—we directly model brightnesses with respect to the  $B$  filters of a fixed photometric system. We designate a particular filter as the “reference” filter, letting the random variable  $r_s$  denote the brightness of object  $s$  with respect to that filter. A priori,

$$(3) \quad r_s | (a_s = i) \sim \text{LogNormal}(\mathcal{R}_{i1}, \mathcal{R}_{i2}).$$

Brightness  $r_s$  is measured in nanomaggies (SDSS 2017), a linear unit; e.g., a light source with twice the nanomaggies as another emits twice as many photons in expectation. The log-normal distribution reflects that brightness is non-negative and that stars’ brightnesses often differ by orders of magnitude. Empirically, a log-normal distribution fits better than any gamma distribution—another common model for non-negative real-valued variables. Our prior depends on  $a_s$  to reflect that stars tend to be brighter than galaxies.

The brightness of light source  $s$  with respect to the remaining  $B - 1$  filters are encoded using colors. The color  $c_{s\beta}$  is defined as the log ratio of brightnesses with respect to filters  $\beta$  and  $\beta + 1$ . Here, the filters are ordered by the wavelength bands they let pass. The  $B - 1$  colors for object  $s$  are collectively denoted by  $c_s$ , a random  $(B - 1)$ -vector. The reference-filter brightness  $r_s$  and the colors  $c_s$  uniquely specify the brightnesses for light source  $s$  in any filter  $\beta$ , denoted  $\ell_s(\beta)$ .

Our model uses the color parameterization because stars and galaxies have very distinct prior distributions in color space. Indeed, for idealized stars—blackbodies—all  $B - 1$  colors lie on a one-dimensional manifold indexed by surface temperature. On the other hand, though galaxies are composed of stars, theory does not suggest they lie near the same manifold: the stars in a galaxy can have many different surface temperatures, and some of the photons are re-processed to other energies through interactions with dust and gas. Figure 3 demonstrates that stars are much closer to a one-dimensional manifold in color space than galaxies are.

We model the prior distribution on  $c_s$  as a  $D$ -component Gaussian mixture model (GMM):

$$(4) \quad c_s | (a_s = i) \sim \text{GMM}(C_i^{weight}, C_i^{mean}, C_i^{cov}).$$



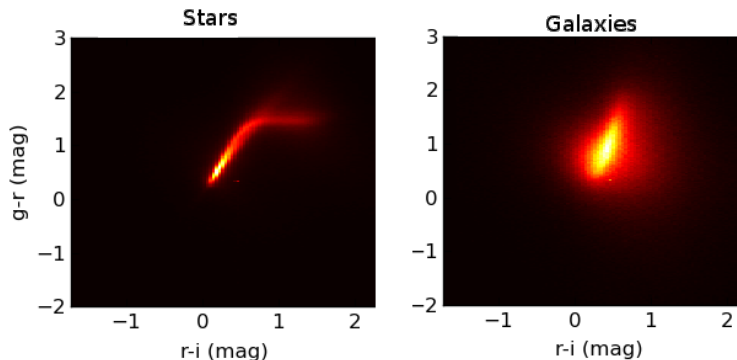


Fig 3: Density plots for two colors,  $g-r$  and  $r-i$ , based on a pre-existing catalog containing hundreds of thousands of stars and galaxies.

In principle,  $D$  could be set with a statistical model selection criterion. In practice, we set  $D = 8$  based on computational considerations, without any apparent accuracy reduction. Because we have so much data (millions of light sources), there is no risk of overfitting with  $D = 8$ : held-out log likelihood improves as  $D$  increases up to  $D = 256$ , the largest setting our hardware allowed us to test. There is also little risk that  $D = 8$  underfits: setting  $D = 16$  does not substantively change our predictions.

**2.1.2. Pointwise brightness.** Consider a light source  $s$ , centered at some sky location  $u_s$ . Its brightness in filter band  $\beta$ , measured at a possibly different sky location  $\mu$ , is given by

$$(5) \quad \varphi_s(\beta, \mu) := \ell_s(\beta) h_s(\mu).$$

Here  $h_s$  (a density) models the spatial characteristics of light source  $s$ , returning the relative intensity at location  $\mu$ , specified in sky coordinates (not image-specific “pixel coordinates”). We refer to  $h_s$  as the “light kernel” for light source  $s$ .

The distance from Earth to any star (besides the Sun) exceeds the star’s radius by many orders of magnitude. Therefore, we model stars as point sources. If light source  $s$  is a star (i.e.,  $a_s = 1$ ), then  $h_s$  is simply a delta function: one if  $\mu = u_s$  and zero otherwise.

Modeling the (two-dimensional) appearance of galaxies as seen from Earth is more involved. If light source  $s$  is a galaxy (i.e.,  $a_s = 0$ ), then  $h_s$  is parameterized by a latent random 4-vector

$$(6) \quad e_s := (e_s^{profile}, e_s^{angle}, e_s^{radius}, e_s^{axis}).$$

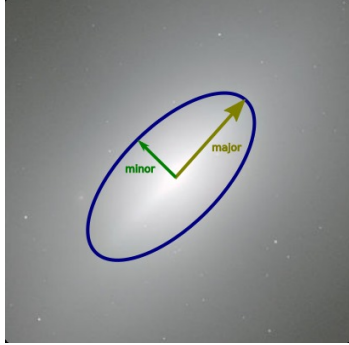


Fig 4: An example of the galaxy model. The blue ellipse surrounds half of the light emissions of this galaxy. The length of the major axis is the half-light radius  $e_s^{scale}$ . The angle in degrees of the major axis is  $e_s^{angle} = 45$ . The ratio of the lengths of minor and major axes is  $e_s^{axis} = 1/2$ . Because this galaxy is purely elliptical,  $e_s^{profile} = 0$ .

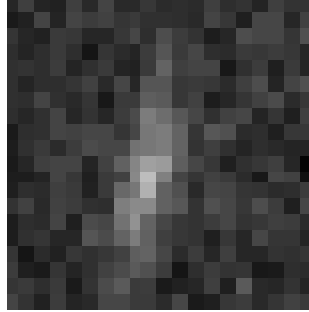
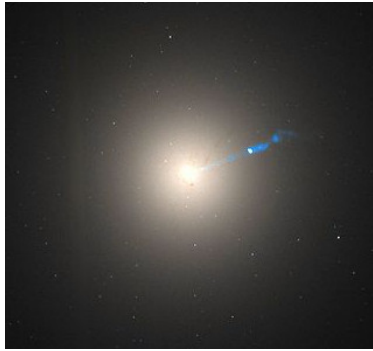


Fig 5: A distant galaxy approximately 20 pixels in height, predicted to have half-light radius  $e_s^{scale} = 0.6$  arcseconds, rotation  $e_s^{angle} = 80$  degrees, and minor-major axis ratio  $e_s^{axis} = 0.17$ .



(a) Messier 87, a galaxy that exhibits the de Vaucouleurs profile. Credit: NASA



(b) Triangulum, a galaxy that exhibits the exponential profile. Credit: NASA

Fig 6: Extremal galaxy profiles

We take  $h_s$  to be a convex combination of two extremal profiles, known in astronomy as “de Vaucouleurs” and “exponential” profiles:

$$(7) \quad h_s(\mu) = e_s^{profile} h_{s1}(\mu) + (1 - e_s^{profile}) h_{s2}(\mu).$$

The de Vaucouleurs profile is characteristic of elliptical galaxies, whose luminosities vary gradually in space (Figure 6a), whereas exponential profile matches spiral galaxies (Figure 6b). The profile functions  $h_{s1}(\mu)$  and  $h_{s2}(\mu)$  also account for additional galaxy-specific parameters illustrated in Figure 4. In particular, each profile function is a rotated, scaled mixture of bivariate normal distributions. Angle and scale are galaxy specific, while the remaining parameters of each mixture are not:

$$(8) \quad h_{si}(\mu) = \sum_{j=1}^J \alpha_{ij} \phi(\mu; u_s, \tau_{ij} \Sigma_s), \quad i = 1 \text{ or } 2.$$

Here the  $\alpha_{ij}$  and the  $\tau_{ij}$  are prespecified constants that characterize the exponential and de Vaucouleurs profiles;  $u_s$  is the center of the galaxy in sky coordinates;  $\Sigma_s$  is a  $2 \times 2$ -covariance matrix shared across the components; and  $\phi$  is the bivariate normal density.

The light kernel  $h_s(\mu)$  is a finite scale mixture of Gaussians: its mixture components have a common mean  $u_s$  and covariance matrices that differ only in scale. The isophotes (level sets of the light kernel) are concentric ellipses. Although this model prevents us from fitting individual “arms,” like those of the galaxy in Figure 6b, most galaxies are not sufficiently resolved to see such substructure. Figure 5 shows a more typical galaxy image.

The spatial covariance matrix  $\Sigma_s$  is parameterized by a rotation  $e_s^{angle}$ , an eccentricity (minor-major axis ratio)  $e_s^{axis}$ , and an overall size scale  $e_s^{scale}$ :

$$(9) \quad \Sigma_s := R_s^\top \begin{bmatrix} [e_s^{scale}]^2 & 0 \\ 0 & [e_s^{axis}]^2 [e_s^{scale}]^2 \end{bmatrix} R_s,$$

where the rotation matrix

$$(10) \quad R_s := \begin{bmatrix} \cos e_s^{angle} & -\sin e_s^{angle} \\ \sin e_s^{angle} & \cos e_s^{angle} \end{bmatrix}.$$

The scale  $e_s^{scale}$  is specified in terms of half-light radius—the radius of the disc that contains half of the galaxy’s light emissions before applying the eccentricity  $e_s^{angle}$ .

All four entries of  $e_s$  are random. The mixing weight prior is given by

$$(11) \quad e_s^{profile} \sim \text{Beta}(\mathcal{E}_1^{profile}, \mathcal{E}_2^{profile}).$$

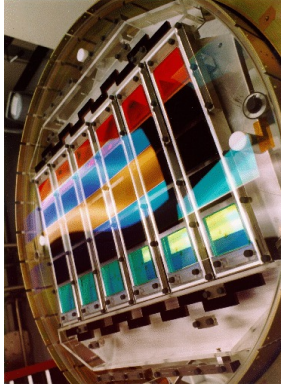


Fig 7: The SDSS camera. Its CCDs—each  $2048 \times 2048$  pixels—are arranged in 6 columns and 5 rows. A different filter covers each row. Credit: [SDSS \(2018a\)](#).

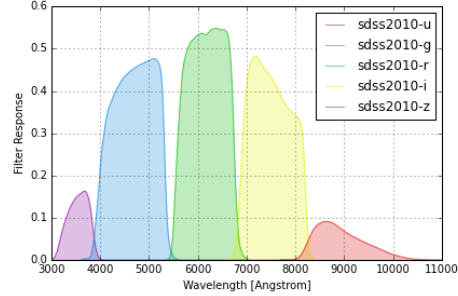


Fig 8: SDSS filter curves. Filter response is the probability that a photon of a particular wavelength will pass through the filter. Credit: [Doi et al. \(2010\)](#).

Every angle is equally likely, and galaxies are symmetric, so

$$(12) \quad e_s^{angle} \sim \text{Uniform}([0, 180]).$$

We found the following distribution to fit well empirically:

$$(13) \quad e_s^{radius} \sim \text{LogNormal}(\mathcal{E}_1^{radius}, \mathcal{E}_2^{radius}).$$

The “fatter” tail of a log-normal distribution fits better than a gamma distribution, for example. A priori, the major-minor axis ratio

$$(14) \quad e_s^{axis} \sim \text{Beta}(\mathcal{E}_1^{axis}, \mathcal{E}_2^{axis}).$$

**2.2. Images.** Astronomical images are taken through telescopes. Photons that enter the telescope reach a camera at its base that records the pixel each photon hits, thus contributing an electron. The SDSS camera (Figure 7) consists of 30 charge-coupled devices (CCDs), arranged in a grid of 6 columns and 5 rows. Each row is covered by a different filter—translucent colored glass that limits what photons can pass through and potentially get recorded. Each of the five filters selects, stochastically, for photons of different wavelengths. The five filters are named for the wavelengths they are most likely to let pass: ultraviolet (u), green (g), red (r), near infrared (i), and infrared (z). Figure 8 shows how likely a photon of particular wavelength is to pass through each filter. Multiple images of the same region of the sky with different filters reveals the colors of stars and galaxies.

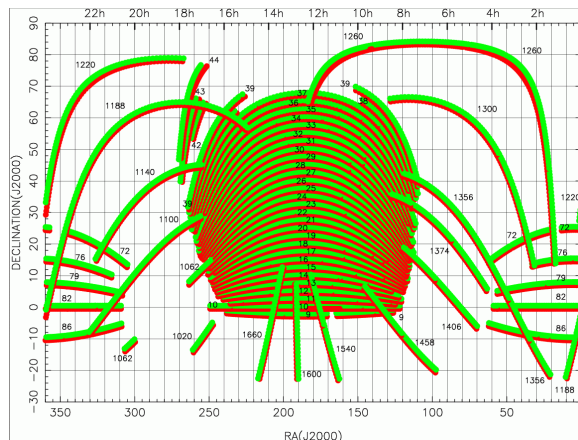


Fig 9: SDSS sky coverage map. Each monochrom arc represents the sky photographed during a particular night. The telescope remains fixed while the Earth rotates. Axes' units are degrees of right ascension (RA) and declination (Dec) with respect to the equator. Credit: [SDSS \(2018b\)](#).

The SDSS telescope collects images by drift scanning, an imaging regime where the telescope remains stationary. Earth's rotation changes the view for the telescope. The region of sky that “drifts by” each night—the region that is imaged—forms an arc (Figure 9).

Each arc is divided into multiple image files. SDSS contains  $N = 4,690,230$  of these images, each taken through a single CCD. For  $n = 1, \dots, N$ , the constant  $\beta_n$  denotes the filter color for image  $n$ .

Each image is a grid of  $M = 2048 \times 1361$  pixels. The observed random variable  $x_{nm}$  denotes the count of photons that, during the exposure for image  $n$ , entered the telescope, passed through the filter, and hit pixel  $m$ .

**2.2.1. Sky brightness.** The night sky is not completely dark, owing to both artificial skyglow (e.g., light pollution from cities) and natural skyglow. Sources of natural skyglow include sunlight reflected off dust particles in the solar system, cosmic microwave background, night airglow from molecules in Earth's atmosphere, and scattered starlight and moonlight. The sky brightness varies by the time of the exposure, due to changing atmospheric conditions. It also varies with sky position; for example, the sky is typically brighter near the galactic plane. We model the night sky's brightness as background noise, through a spatial Poisson process whose rate varies gradually by pixel, independent of stars and galaxies.

The noise rate for each pixel is estimated during preprocessing and fixed

during inference. For the vast majority of pixels, the sky background is their only source of photons. Sky intensity is estimated by pre-existing software (Bertin & Arnouts 1996). This software fits a smooth parametric model to the intensities of the pixels which it determines are not near any light source. The sky intensity could, instead, be fit within our inference procedure. However, the existing estimates of sky intensity are highly accurate, so this is not urgent future work.

The sky intensity for image  $n$  is stored as a grid of  $Q$  intensities in the matrix  $\sigma_n$ . Typically  $Q \ll M$  because the sky intensity varies slowly. To form the sky intensity for a particular pixel,  $\sigma_n$  is interpolated linearly. We denote the sky intensity for a particular pixel  $\sigma_n(m)$ .

*2.2.2. Point-spread functions.* Astronomical images are blurred by a combination of small-angle scattering in Earth’s atmosphere, the diffraction limit of the telescope, optical distortions in the camera, and charge diffusion within the silicon of the CCD detectors. Together these effects are represented by the point spread function (PSF) of a given image. Stars are essentially point sources, but the PSF represents how their photons are spread over dozens of adjacent pixels.

The PSF is set during preprocessing by pre-existing software (Lupton et al. 2001) that identifies several bright stars in each image whose brightness and sky location are known from previous study by spectrographs. The accuracy of spectrographs far exceeds images, so spectrographic values are essentially exact for our purposes. As with sky brightness, in principle we could fit the PSF jointly with light sources through our approximate inference procedure. In practice, the PSF is not our most significant source of model misspecification. Replacing the pre-existing PSF-fitting software would require substantial software-engineering labor, yet may not substantially improve our model, so it is not our highest priority for future work.

The PSF is specified through several image-specific parameters that are bundled together in  $\psi_n$ . The vector  $\psi_n^{calib}$  gives the expected number of photons per nanomaggy for each column of image  $n$ . The vector  $\psi_n^{wcs}$  specifies a mapping from sky location to pixel location. This mapping is linear—an approximation that holds up well locally. The rows of the matrix  $\psi_n^{image}$  give the top principal components from an eigendecomposition of the PSF as rendered on a grid centered at a light source. The vector  $\psi_n^{weight}$  gives the loading of the PSF at any point in the image. It has smooth spatial variation.

We denote the expected contribution of photons from a one nanomaggy star at sky location  $\mu$  to pixel  $m$  of image  $n$  as  $\psi_n(m, \mu)$ ; it is derived as needed from the explicitly represented quantities discussed above.

2.2.3. *The likelihood.* Let  $z_s := (a_s, r_s, c_s, e_s, u_s)$  denote the latent random variables for light source  $s$ . Let  $z := \{z_s\}_{s=1}^S$  denote all the latent random variables. Then, for a given astronomical catalog, the likelihood of pixel  $m$  in image  $n$  is

$$(15) \quad x_{nm}|z \sim \text{Poisson}(\lambda_{nm}).$$

The rate parameter  $\lambda_{nm}$  is unique to that pixel. It is a deterministic function of the catalog (which includes random quantities) given by

$$(16) \quad \lambda_{nm} := \sigma_n(m) + \sum_{s=1}^S \ell_s(\beta) \int \psi_n(m, \mu) h_s(\mu) d\mu.$$

The summation over light sources implies that light sources do not occlude one another, or the sky background. The integral is over all sky locations. In practice it can be restricted to locations near pixel  $m$ —distant light sources contribute a negligible number of photons. As shorthand, we denote the integral as

$$(17) \quad f_{nms} := \int \psi_n(m, \mu) h_s(\mu) d\mu.$$

If light source  $s$  is a star, then it is straightforward to express  $f_{nms}$  analytically:

$$(18) \quad f_{nms} = \psi_n(m, u_s).$$

If light source  $s$  is a galaxy, the same integral is more complex because galaxies have spatial extent. We approximate it by approximating  $\psi_n$  with a linear combination of bivariate normal densities. Because Gaussian-Gaussian convolution is analytic, we get an analytic approximation to  $f_{nms}$ .

Our primary use for the model is computing the posterior distribution of its unobserved random variables conditional on a particular collection of astronomical images. We denote the posterior by  $p(z|x)$ , where  $x := \{x_{nm}\}_{n=1, m=1}^{N, M}$  represents all the pixels. Exact posterior inference is computationally intractable for the proposed model, as it is for most non-trivial Bayesian models. The next two sections consider two approaches to approximate posterior inference: Markov chain Monte Carlo (MCMC) and variational inference (VI).

**3. Markov chain Monte Carlo.** Markov chain Monte Carlo (MCMC) is a common approach for approximating posterior distributions in computationally challenging Bayesian models. MCMC draws samples from a stochastic process on the parameter space whose equilibrium distribution is the posterior distribution of interest. The stochastic process is specified by a transition kernel, denoted  $\mathcal{T}$ . The empirical distribution of these samples approximates the posterior distribution. Statistics of this empirical distribution, such as its mean and its quantiles, approximate the same statistics of the posterior distribution.

Our problem presents two unique challenges for MCMC. First, the state space is extremely high dimensional—there are multiple random variables for each of millions of light sources. We cannot consider transition kernels that require hand-tuning of dimension-specific parameters, such as step size, proposal variance, or temperature schedule. Second, the state space is trans-dimensional. Galaxies have more parameters than stars, and light sources’ types (star vs. galaxy) are themselves random.

We propose a multi-level sampling procedure. In an outer loop based on (block) Gibbs sampling (Bishop 2006), each light source’s latent variables are sampled sequentially, with any overlapping light sources’ latent variables, denoted  $z_{-s}$ , held fixed. Formally, for Gibbs iteration  $k = 1, \dots, K$ , we draw

$$(19) \quad z_s^{(k)} \sim p(z_s | x, z_{-s})$$

for light source  $s = 1, \dots, S$ . We initialize  $z_1^{(0)}, \dots, z_S^{(0)}$  with either a draw from the prior or—to speed up convergence—with approximately correct values determined by a pre-processing routine.

The inner loop, based on annealed importance sampling (AIS) (Neal 2001), is our procedure for drawing from  $p(z_s | x, z_{-s})$ .

3.1. *Estimating the model evidence.* First, we use AIS to estimate

$$(20) \quad p(a_s = 1 | x, z_{-s}).$$

Recall  $a_s$  is the Bernoulli random variable that indexes the source type (star/galaxy), and thus the dimension of our state space. AIS allows us to avoid using a trans-dimensional sampler like reversible-jump MCMC (Green 1995), a technique that often requires constructing a possibly complex trans-dimensional proposal function to generate an efficient Markov chain (Fan & Sisson 2011).

AIS is an iterative procedure to estimate the normalizing constant of an unnormalized probability density  $\pi$ . We set

$$(21) \quad \pi(z_s) := p(x | z_s, a_s = 1, z_{-s}) p(z_s | a_s = 1, z_{-s}).$$



The normalizing constant of  $\pi$  is  $p(x|a_s = 1, z_{-s})$ . Given an estimate of  $p(x|a_s = 1, z_{-s})$ , we can estimate  $p(a_s = 1|x, z_{-s})$  using Bayes's rule.

In addition to the target  $\pi$ , AIS takes as input a sequence of  $T$  distributions  $\pi_0, \pi_1, \dots, \pi_T$  that approach the target. The statistical efficiency of AIS depends on the similarity of intermediate distributions  $\pi_{t-1}(z_s)/\pi_t(z_s)$ . We set  $\pi_0(z_s) := p(z_s|a_s = 1, z_{-s})$ —a normalized density. For  $t = 1, \dots, T$ , we set

$$(22) \quad \pi_t(z_s) = \pi_0(z_s)^{1-\beta_t} \pi(z_s)^{\beta_t}$$

for a sequence of temperatures  $0 = \beta_0 < \beta_1 < \dots < \beta_T = 1$ . These (unnormalized) distributions interpolate between the prior and the posterior.

For  $t = 1, \dots, T$ , let  $\mathcal{T}_t$  be a Markov chain transition that leaves (the normalized version of)  $\pi_t$  invariant. We use slice-sampling-within-Gibbs for the transitions—a procedure requiring no tuning that nonetheless adapts to variable scales for different dimensions (Neal 2003).

We begin by sampling  $z_s^{(0)} \sim \pi_0$ . Then, for  $t = 1, \dots, T$ , we draw

$$(23) \quad z_s^{(t)} | z_s^{(t-1)} \sim \mathcal{T}_t(z_s^{(t-1)}, z_s^{(t)}).$$

After  $T$  iterations,  $z_s^{(T)}$  is approximately distributed according to (the normalized version of)  $\pi_T = \pi$ , and

$$(24) \quad \mathcal{Z}_s := \exp \sum_{t=1}^T \log \frac{\pi_t(z_s^{(t-1)})}{\pi_{t-1}(z_s^{(t-1)})}$$

is a consistent estimator of  $p(x|a_s = 1, z_{-s})$  (Neal 2001).

**3.2. Sampling with AIS.** The final step of our AIS procedure draws samples from  $p(z_s|x, z_{-s})$ . For each source type (star/galaxy), we run  $N$  independent repetitions of our AIS procedure. We use the resulting samples as independent starting positions for  $N$  Markov chains. We run these  $N$  chains for  $B$  more steps, monitoring convergence and mixing criteria (Gelman & Rubin 1992). This process yields  $N$  estimates of the model evidence, and  $N \times B$  (correlated) samples drawn from the Markov chain.

**4. Variational inference.** Variational inference (VI) chooses an approximation to the posterior distribution  $p(z|x)$  from a class of candidate distributions via numerical optimization (Blei et al. 2017). The candidate approximating distributions  $q_\theta(z)$  are parameterized by a real-valued vector  $\theta$ . VI minimizes (with respect to  $\theta$ ) the KL divergence between  $q_\theta(z)$ , called “variational distributions,” and the posterior distribution  $p(z|x)$ .

4.1. *The variational distributions.* We restrict the variational distributions to a class that makes KL minimization tractable. Our variational distributions all factorize:

$$(25) \quad q_\theta(z) = \prod_{s=1}^S q(a_s)q(u_s)q(e_s)q(r_s|a_s)q(c_s|a_s).$$

This is not quite mean-field variational inference (Blei et al. 2017) because several factors are conditional on  $a_s$  (i.e., whether a light source is a star or a galaxy). We have suppressed the subscript  $\theta$  in the variational factors. The next equations show the constituents of  $\theta$ . We use “acute” and “hat” accents to denote variational parameters. For  $s = 1, \dots, S$  and  $i \in \{0, 1\}$  we suppose

$$(26) \quad q(a_s) \sim \text{Bernoulli}(\acute{a}_s),$$

$$(27) \quad q(r_s|a_s = i) \sim \text{LogNormal}(\acute{r}_{si}, \hat{r}_{si}),$$

$$(28) \quad q(c_s|a_s = i) \sim \text{MvNormal}(\acute{c}_{si}, I\hat{c}_{si}),$$

$$(29) \quad q(u_s) \sim \text{PointMass}(\acute{u}_s),$$

$$(30) \quad q(e_s) \sim \text{PointMass}(\acute{e}_s).$$

Here  $\acute{e}_s := (\acute{e}_s^{angle}, \acute{e}_s^{radius}, \acute{e}_s^{profile}, \acute{e}_s^{axis})$ .

4.2. *The variational lower bound.* Because  $p(x)$  is constant wrt  $\theta$ , Minimizing  $D_{\text{KL}}(q_\theta(z), p(z|x))$  is equivalent to maximizing

$$(31) \quad \mathcal{L}(\theta) = \mathbb{E}_{q_\theta} [\log p(x|z)] - D_{\text{KL}}(q_\theta(z), p(z)).$$

Maximization of  $\mathcal{L}(\theta)$  is the standard approach; see Blei et al. (2017) for discussion.

The first term of  $\mathcal{L}(\theta)$  is the expected log likelihood of the data. It is

$$(32) \quad \mathbb{E}_q [\log p(x|z)] = \sum_{n=1}^N \sum_{m=1}^M \{-\mathbb{E}_q [\lambda_{nm}] + x_{nm} \mathbb{E}_q [\log \lambda_{nm}] - \log(x_{nm}!)\}.$$

4.2.1. *Expectation of the rate parameter.* The first expectation is

$$(33) \quad \mathbb{E}_q[\lambda_{nm}] = \sigma_{nm} + \sum_{s=1}^S \mathbb{E}_q[\ell_s(\beta_n) f_{nms}].$$

We can factorize the right-hand expectation based on the factorization of the variational distribution, upon conditioning on  $a_s$ :

$$(34) \quad \begin{aligned} \mathbb{E}_q[\ell_s(\beta_n) f_{nms}] &= (1 - \acute{a}_s) \mathbb{E}_q[\ell_s(\beta_n) | a_s = 0] \mathbb{E}_q[f_{nms} | a_s = 0] \\ &\quad + \acute{a}_s \mathbb{E}_q[\ell_s(\beta_n) | a_s = 1] \mathbb{E}_q[f_{nms} | a_s = 1]. \end{aligned}$$

The integral  $\mathbb{E}_q[\ell_s(\beta) | a_s]$  is tractable because brightness  $r_s$  and each entry of  $c_s$  (the colors) are independent in the variational distribution given  $a_s$ . The integral  $\mathbb{E}_q[f_{nms} | a_s]$  is tractable because  $u_s$  is a point mass in the variational distribution.

4.2.2. *Expectation of the log rate parameter.* We approximate the expected logarithm of  $\lambda_{nm}$  using the delta method for moments (Bickel & Doksum 2015). We replace the integrand with a second-order Taylor expansion around its mean:

$$(35) \quad \begin{aligned} \log(\lambda_{nm}) &\approx \log \mathbb{E}_q[\lambda_{nm}] + \frac{1}{\mathbb{E}_q[\lambda_{nm}]} (\lambda_{nm} - \mathbb{E}_q[\lambda_{nm}]) \\ &\quad - \frac{1}{2\mathbb{E}_q[\lambda_{nm}]^2} (\lambda_{nm} - \mathbb{E}_q[\lambda_{nm}])^2. \end{aligned}$$

Then, taking expectations,

$$(36) \quad \mathbb{E}_q[\log(\lambda_{nm})] \approx \log \mathbb{E}_q[\lambda_{nm}] - \frac{\mathbb{V}_q[\lambda_{nm}]}{2\mathbb{E}_q[\lambda_{nm}]^2},$$

where  $\mathbb{V}_q$  denotes variance with respect to the variational distribution  $q$ . That term may be further expanded:

$$(37) \quad \mathbb{V}_q[\lambda_{nm}] = \sum_{s=1}^S \mathbb{V}_q[\ell_s(\beta_n) f_{nms}]$$

$$(38) \quad = \sum_{s=1}^S \mathbb{E}_q[\ell_s(\beta_n)^2 f_{nms}^2] + \mathbb{E}_q[\ell_s(\beta_n) f_{nms}]^2.$$

The second expectation on the right-hand side is given in Equation 34. The first is

$$(39) \quad \begin{aligned} \mathbb{E}_q[\ell_s(\beta_n)^2 f_{nms}^2] &= (1 - \acute{a}_s) \mathbb{E}_q[\ell_s(\beta_n)^2 | a_s = 0] \mathbb{E}_q[f_{nms}^2 | a_s = 0] \\ &\quad + \acute{a}_s \mathbb{E}_q[\ell_s(\beta_n)^2 | a_s = 1] \mathbb{E}_q[f_{nms}^2 | a_s = 1]. \end{aligned}$$

4.2.3. *KL divergence.* Because of the factorization of the variational distribution, the KL term separates across sources:

$$(40) \quad D_{\text{KL}}(q(z), p(z)) = \sum_{s=1}^S D_{\text{KL}}(q(z_s), p(z_s)).$$

It separates further within each source:

$$(41) \quad \begin{aligned} D_{\text{KL}}(q(z_s), p(z_s)) &= D_{\text{KL}}(q(a_s), p(a_s)) \\ &+ D_{\text{KL}}(q(u_s), p(u_s)) + D_{\text{KL}}(q(e_s), p(e_s)) \\ &+ \sum_{i=0}^1 q(a_s = i) \left[ D_{\text{KL}}(q(r_s|a_s = i), p(r_s|a_s = i)) \right. \\ &\quad \left. + D_{\text{KL}}(q(c_s|a_s = i), p(c_s|a_s = i)) \right]. \end{aligned}$$

Except for the last, these KL divergences are between common exponential family distributions. We give formulas for them in Appendix A.

The last KL divergence is more complicated because the prior on  $c_s$  is a Gaussian mixture model. We take the eighth approach from [Hershey & Olsen \(2007\)](#) to identify an upper bound on this KL divergence:

$$(42) \quad \begin{aligned} D_{\text{KL}}(q(c_s|a_s = i), p(c_s|a_s = i)) \\ \leq D_{\text{KL}}(\xi_i, C_i^{\text{weights}}) + \sum_{j=1}^J \xi_{ij} D_{\text{KL}}(q(c_s|a_s = i), C_{ij}). \end{aligned}$$

Here  $C_i^{\text{weights}}$  is the categorical distribution over the color prior’s mixture components,  $C_{ij}$  is the color prior’s  $j$ th mixture component, and  $\xi_i \in [0, 1]^J$  is a vector of free parameters. To make the bound as tight as possible, we optimize  $\xi$  along with the variational lower bound. The optimal  $\xi$  can also be expressed analytically:

$$(43) \quad \xi_{ij}^* \propto C_{ij}^{\text{weights}} \exp\{-D_{\text{KL}}(q(c_s|a_s = i), C_{ij})\}.$$

4.3. *Numerical optimization.* Traditionally, variational lower bounds are maximized through coordinate ascent: each update sets a variational parameter to its optimal value with the others held fixed ([Bishop 2006](#), [Murphy 2012](#)). This approach is simple to implement because gradients and Hessians do not need to be explicitly computed. Each update increases the variational lower bound. The algorithm converges to a local optimum even for nonconvex objective functions. However, coordinate ascent can take many iterations to

converge when the Hessian of the objective function is not diagonal. Additionally, for many models, including ours, optimal coordinate ascent updates cannot be expressed analytically.

Instead, we propose an optimization procedure based on *block* coordinate ascent. Each light source corresponds to a block of 44 variational parameters. We optimize each block by calling a subsolver, explained in the next paragraph. Because most pairs of light sources do not overlap, the Hessian has low fill off the block diagonal. Block coordinate ascent converges quickly in this setting: for light sources that do not overlap with any other light source, just one update step, based on one call to a subsolver, is required to reach a local maximum. For groups of light sources that overlap with each other, a few passes over each light source suffice in practice. Light sources may be optimized in a round-robin order or at random.

As a subsolver to optimize one block of parameters with all others fixed, we use Newton’s method with a trust-region constraint (Nocedal & Wright 1999). The trust-region constraint ensures that we find a local maximum even though the variational objective is nonconvex. The method consistently converges in tens of iterations, whereas first-order methods take thousands. BFGS (Nocedal & Wright 1999) also on occasion required thousands of iterations per call. Newton iterations are more expensive computationally than first-order methods’ iterations because the former requires computing a dense Hessian along with each gradient. For our objective function, computing both a Hessian and a gradient takes  $3\times$  longer than computing a gradient alone. In the end, we gain at least an order of magnitude speedup by using Newton’s method rather than a gradient-only method because the former requires many fewer iterations.

4.4. *Distributed optimization.* Modern compute clusters and supercomputers contain many individual *compute nodes* that execute instructions in parallel. Additionally, each compute node runs many *threads* in parallel—at least one per CPU core. Communication among compute nodes is orders of magnitude slower than communication among threads on the same node.

Block coordinate ascent (the outer loop of our optimization procedure) is a serial algorithm: if multiple blocks of parameters are updated simultaneously based on the current iterate, the objective value may decrease, and the algorithm may diverge. By taking of advantage of the structure of our problem, however, we parallelize block coordinate ascent across both compute nodes and CPU cores. Equation 32 is a sum over pixels and Equation 40 is a sum over light sources. Therefore, our objective function may be expressed as a sum whose terms each depend on the parameters for at most one light

source from any particular collection of non-overlapping light sources. Thus, for any collection of non-overlapping light sources, maximizing over each light source's parameters serially is equivalent to maximizing over all these light sources' parameters in parallel.

Each compute node is tasked with optimizing all the light sources in a region of the sky. Because these light sources are physically near each other, they appear in many of the same images; we only need to load these images once for all them. Each node implements a locking mechanism that prevents its threads from optimizing overlapping light sources simultaneously. Because within-node communication is fast, there is essentially no overhead from this type of locking mechanism.

Communication between nodes is relatively slow. We avoid using an inter-node locking mechanism by assigning each node to optimize different regions of the sky. Because the boundaries of these regions are small relative to the interior, we approximately find a stationary point with this approach. A second pass with slightly different boundaries ensures that even light sources near a boundary are fully optimized.

**5. Experimental results.** Our experiments use both synthetic images drawn from our model (Section 5.1) and images from the Sloan Digital Sky Survey (Section 5.2). For both datasets, we run both the MCMC procedure from Section 3 (henceforth, MCMC) and the variational inference procedure from Section 4 (henceforth, VI), and compare their posterior approximations. We assess the accuracy of point estimates (e.g., posterior means/modes) and uncertainties (e.g., posterior variances), as well as star/galaxy classification accuracy.

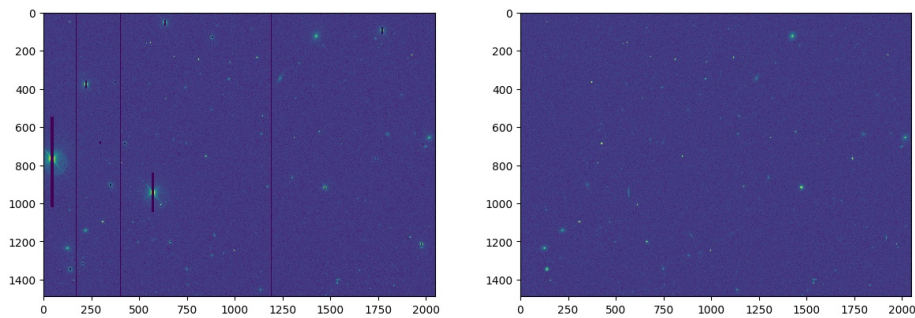


Fig 10: *Left*: An image from SDSS containing approximately 1000 detectable light sources. Pixels in error are “masked.” *Right*: A synthetic image for the same region, generated from our model by conditioning on the real image’s catalog, with several of the brightest light sources removed.

5.1. *Synthetic images.* Synthetic images let us compare inference methods without model misspecification, with known “ground truth” for latent random variables. Synthetic images also let us validate our model by visually checking their similarity to real images. To generate realistic synthetic images, we take the non-inferred parameter values from real SDSS images, including the point spread function  $\psi_n$ , the sky background  $\sigma_n$ , and structural constants like the dimensions of the images. To illustrate that synthetic data

	within 1/2 sd	1 sd	2 sd	3 sd		within 1/2 sd	1 sd	2 sd	3 sd
log brightness	0.18	0.31	0.55	0.68	log brightness	0.36	0.64	0.92	0.99
color u-g	0.29	0.52	0.79	0.89	color u-g	0.43	0.73	0.95	1.00
color g-r	0.26	0.46	0.71	0.80	color g-r	0.41	0.68	0.93	0.99
color r-i	0.22	0.43	0.72	0.84	color r-i	0.41	0.67	0.94	0.99
color i-z	0.32	0.58	0.82	0.93	color i-z	0.41	0.71	0.93	0.99

Table 5: Proportion of light sources having posterior means found by VI (left) and MCMC (right) near the ground truth for synthetic images.

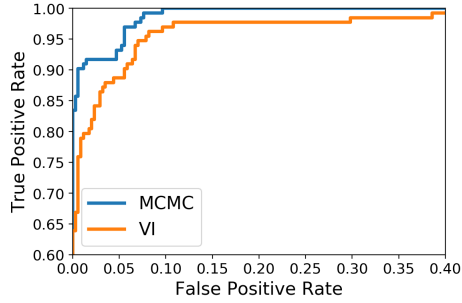


Fig 11: ROC curve for star/galaxy classification on synthetic data.

	MCMC	VI	VI-MCMC
position	0.111	0.121	<b>0.010</b> ( $\pm 0.003$ )
brightness	0.093	0.118	<b>0.025</b> ( $\pm 0.006$ )
color u-g	0.327	0.333	0.006 ( $\pm 0.008$ )
color g-r	0.128	0.126	-0.002 ( $\pm 0.004$ )
color r-i	0.112	0.110	-0.002 ( $\pm 0.005$ )
color i-z	0.154	0.144	-0.010 ( $\pm 0.005$ )
galaxy profile	0.158	0.229	<b>0.072</b> ( $\pm 0.011$ )
galaxy axis	0.074	0.106	<b>0.032</b> ( $\pm 0.006$ )
galaxy radius	0.450	0.688	<b>0.237</b> ( $\pm 0.043$ )
galaxy angle	9.642	8.943	-0.699 ( $\pm 0.437$ )

Table 4: Left columns: Mean absolute error on synthetic data. **Lower is better.** Right column: Pairwise error differences (and standard error). Statistically significant differences appear in bold font.

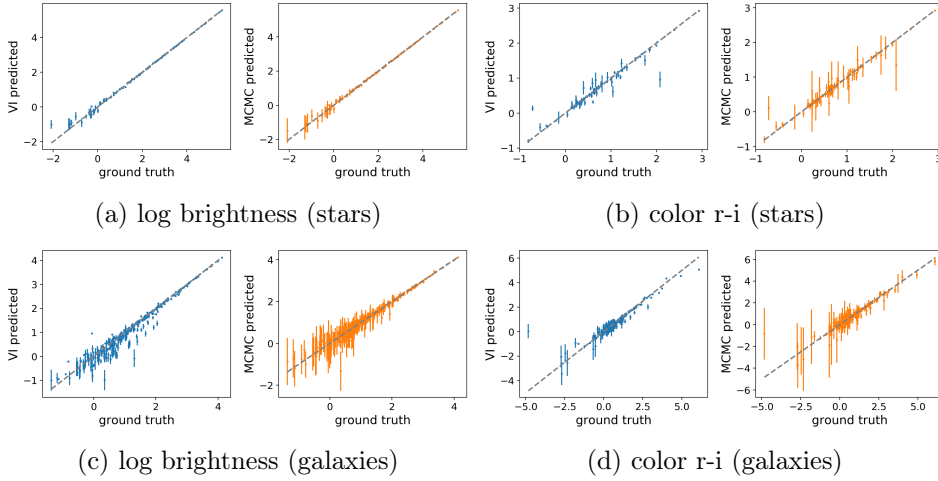


Fig 12: VI and MCMC performance on synthetic data. Each pair depicts VI (left, blue), and MCMC (right, orange), with the ground truth along the  $x$ -axis and the posterior distribution (showing two standard deviations) along the  $y$ -axis.



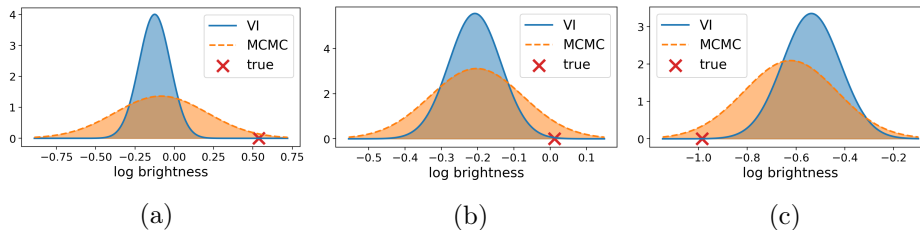


Fig 13: Comparison of posterior uncertainty for the brightness of three synthetic light sources where the posterior mean is a poor prediction of the true parameter value. VI underestimates posterior uncertainty. MCMC assigns much more posterior mass to the true values.

resemble real images, Figure 10 depicts a synthetic image generated using parameters from an existing catalog. In our experiments, the light sources in synthetic images are instead drawn from the prior. Our synthetic study set comprises five overlapping  $2048 \times 1489$ -pixel images. Each image is for a different filter band. The images contain approximately 500 detectable light sources.

Empirically, MCMC performs better at star/galaxy classification than VI for all thresholds of a receiver operating characteristic (ROC) curve (Figure 11). Both methods have a high area under the curve (AUC). For MCMC, the AUC is 0.994. For VI, the AUC is 0.981.

Both methods estimate means well for all continuous latent random variables (Table 4). MCMC outperforms VI slightly for some point estimates. “Position” is error, in arcseconds (0.396 pixels), for the location of the light sources’ centers. “Brightness” measures the reference band (r-band) brightness. “Colors” are ratios of magnitudes in consecutive bands. “Galaxy profile” is a proportion indicating whether a galaxy is de Vaucouleurs or exponential. “Galaxy axis” is the ratio between the lengths of a galaxy’s minor and major axes. “Galaxy radius” is the half-light radius of a galaxy in arcseconds. “Galaxy angle” is the orientation of a galaxy in degrees.

For color and brightness, MCMC often has larger posterior uncertainty. MCMC assigns substantial probability to the truth more often than VI (Figure 12). For light sources where posterior means are particularly poor predictors of the truth, VI severely underestimates the uncertainty, whereas MCMC assigns much more posterior mass to the true values (Figure 13). For color and log brightness—both normally distributed quantities—errors from MCMC are more nearly normally distributed than those of VI (Table 5).

These empirical results are anticipated by theory: VI underestimates the

posterior uncertainty because independence assumptions in the variational distribution do not hold in the posterior (Bishop 2006).

5.2. *Real images from SDSS.* Absolute truth is unknowable for astronomical catalogs. Fortunately, one area of the sky, called “Stripe 82,” has been imaged 80 times in SDSS, whereas most regions have been imaged just once. This region provides a convenient validation strategy: combine exposures from all Stripe-82 runs to produce a high signal-to-noise image, and estimate ground truth parameters from that image.

Photo (Lupton et al. 2005) is a state-of-the-art software pipeline for constructing large astronomical catalogs. Photo is a carefully hand-tuned heuristic. We use Photo’s estimated parameters from the combined Stripe 82 imagery as ground truth. We then run Photo and our method on just one of the 80 image sets, comparing the results from each to the ground truth. Although this “ground truth” is still prone to errors, such errors typically favor Photo, since any systematic errors will be consistent in Photo’s output.

To reduce the runtime of our algorithms, we test them on only a subset of Stripe 82. Our Stripe 82 study set comprises five overlapping  $2048 \times 1489$ -pixel images for a typical region of sky. Each of these image is for a different filter band. The images contain approximately 500 detectable light sources.

For star/galaxy classification in SDSS data, MCMC outperforms VI at some thresholds, and performs slightly worse than VI at others (Figure 14). In addition to point estimates, our inference procedures approximate posterior uncertainty for source type (star or galaxy), brightness, and colors. This is a novel feature of a Bayesian approach, offering astronomers a principled measure of the quality of inference for each light source. No such analogue exists for Photo.

Table 6 is our main empirical result. It quantifies point estimate error from MCMC and VI for the real-valued latent random variables, as well as a pairwise error comparison between each method. MCMC and VI both substantially outperform Photo. Both make especially large improvements at estimating color. Only our model has a prior on color. Photo estimates band brightness independently for each light source.

Point estimate error for MCMC and VI differed significantly only for galaxy profile and galaxy axis ratio. For galaxy axis, MCMC outperformed VI, repeating our experience with synthetic data. For galaxy profile, however, VI outperformed MCMC—the opposite of how the methods compared on synthetic data. Sampler diagnostics—though not conclusive—suggest that insufficient mixing was not to blame. Model misfit—though an obvious explanation for any result not shared by synthetic data—seems inadequate

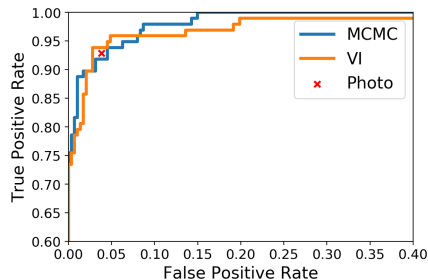


Fig 14: The receiver operating characteristic (ROC) curve for star/galaxy classification on Stripe 82 data. The area under the curve (AUC) for MCMC is 0.991 and for VI is 0.985.

because MCMC recovered the other galaxy shape parameters at least as well as VI.

Our leading explanation is that “ground truth” is unreliable for galaxy profile, and that VI more accurately recreates its mistakes. Recall ground truth is determined by additively combining many overlapping images. These images were taken through a variety of atmospheric conditions. Errors in the point spread function (PSF) are likely compounded by the addition of more data. Galaxy profile may be particularly susceptible to errors in the PSF because it has the capacity to model image blur that should have been attributed to the PSF.

For SDSS images, MCMC had better calibrated uncertainty estimates, particularly for log brightness (Figure 15, Figure 16, and Table 7). Recall that on the synthetic data, MCMC substantially outperformed VI at modeling uncertainty, producing empirical uncertainties that followed their theoretical distribution almost exactly (Figure 5). On real data, uncertainty estimates for both MCMC and VI are worse than on synthetic data. Model misspecification appears to be more significant than the bias introduced by the independence assumptions of the variational distribution.

*5.3. Runtime comparison.* MCMC took approximately  $1000\times$  longer in wall-clock time than VI to attain good results. The implementations for MCMC and VI were both carefully optimized for speed, to make comparing runtimes fair. In fact, the majority of runtime for MCMC was spent in code VI also used, since the most computationally intensive calculations (across pixels) are shared by both the variational lower bound and the log probability. That largely rules out “implementation differences” as an explanation for the disparity in runtime.

	MCMC	VI	Photo	Photo-VI	Photo-MCMC	VI-MCMC
position	0.266	0.268	0.271	0.003 ( $\pm$ 0.011)	0.004 ( $\pm$ 0.010)	0.001 ( $\pm$ 0.002)
brightness	0.163	0.159	0.168	0.009 ( $\pm$ 0.013)	0.005 ( $\pm$ 0.013)	-0.005 ( $\pm$ 0.008)
color u-g	0.574	0.589	0.943	<b>0.417</b> ( $\pm$ 0.063)	<b>0.428</b> ( $\pm$ 0.063)	0.015 ( $\pm$ 0.008)
color g-r	0.146	0.146	0.293	<b>0.147</b> ( $\pm$ 0.020)	<b>0.147</b> ( $\pm$ 0.019)	0.0005 ( $\pm$ 0.003)
color r-i	0.096	0.097	0.175	<b>0.078</b> ( $\pm$ 0.010)	<b>0.079</b> ( $\pm$ 0.010)	0.001 ( $\pm$ 0.002)
color i-z	0.158	0.153	0.336	<b>0.184</b> ( $\pm$ 0.026)	<b>0.179</b> ( $\pm$ 0.026)	-0.005 ( $\pm$ 0.003)
galaxy profile	0.268	0.195	0.245	<b>0.050</b> ( $\pm$ 0.019)	-0.023 ( $\pm$ 0.018)	<b>-0.073</b> ( $\pm$ 0.015)
galaxy axis	0.115	0.146	0.219	<b>0.073</b> ( $\pm$ 0.012)	<b>0.104</b> ( $\pm$ 0.012)	<b>0.031</b> ( $\pm$ 0.005)
galaxy radius	0.572	0.692	1.274	0.582 ( $\pm$ 0.299)	<b>0.701</b> ( $\pm$ 0.293)	0.120 ( $\pm$ 0.067)
galaxy angle	19.32	19.54	20.39	0.838 ( $\pm$ 1.164)	1.062 ( $\pm$ 1.165)	0.225 ( $\pm$ 0.549)

Table 6: *Left columns*: Mean absolute error on Stripe 82 data. **Lower is better**. *Right columns*: Pairwise error differences for each pair of methods (and standard error). Statistically significant differences appear in bold font.

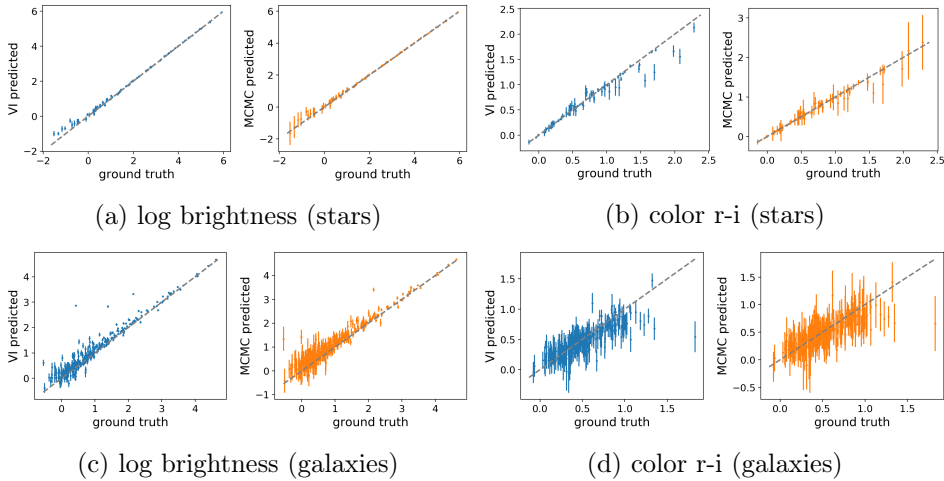


Fig 15: VI and MCMC performance on real data from Stripe 82. Each pair depicts VI (left, blue), and MCMC (right, orange), with the ground truth along the  $x$ -axis and the posterior distribution (showing two standard deviations) along the  $y$ -axis.

	within 1/2 sd	1 sd	2 sd	3 sd		within 1/2 sd	1 sd	2 sd	3 sd
log brightness	0.12	0.21	0.39	0.58	log brightness	0.18	0.37	0.67	0.82
color u-g	0.25	0.44	0.75	0.89	color u-g	0.30	0.57	0.85	0.91
color g-r	0.25	0.48	0.76	0.91	color g-r	0.34	0.59	0.85	0.94
color r-i	0.22	0.41	0.72	0.87	color r-i	0.30	0.58	0.88	0.95
color i-z	0.27	0.51	0.81	0.94	color i-z	0.33	0.57	0.87	0.95

Table 7: Proportion of light sources having posterior means found by VI (left) and MCMC (right) near the ground truth for SDSS images.

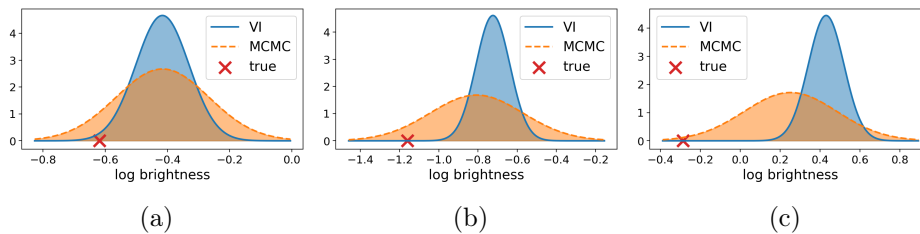


Fig 16: Comparison of posterior uncertainty for the brightness of three light sources from Stripe 82 where the posterior mean is a poor prediction of the true parameter value. VI underestimates posterior uncertainty. MCMC assigns much more posterior mass to the true values.

The same hardware was used for all timing experiments: a single core of an Intel Xeon E5-2698 v3 clocked at 2.30GHz.

Our MCMC experiments use a temperature schedule of length 200 for annealed importance sampling (AIS). We repeated AIS 25 times to generate 25 independent estimates of the normalizing constant for each model. We then ran each of those 25 independent posterior samples for 25 more slice sampling steps, generating 625 total correlated samples. For MCMC, the number of correlated samples drawn scales linearly with runtime, presenting a speed/accuracy trade off. However, the quality of an MCMC posterior approximation is a function of the number of effectively independent samples (Gelman et al. 2014). We measure the rate at which slice sampling is able to compute effectively independent samples for a single source ( $52 \times 52$  image patch). For star objects, we compute about 0.225 effectively independent samples per second. For galaxies, it is 0.138 effectively independent samples per second.

VI is able to compute an approximate posterior distribution in roughly 9 seconds. To generate at least 100 effectively independent star and galaxy samples requires roughly  $100 \times$  the computation required to compute the VI approximation. This tally ignores the amount of time it takes to generate the AIS normalizing constant estimate, which more than doubles the amount of time spent in the algorithm.

**6. Bayesian inference at petascale.** Catalog inference is a “big data” problem that does not parallelize trivially. This section introduces high-performance computing (HPC) to a statistics audience by describing large-scale runs of our variational inference procedure. We construct a catalog from the entire 50-terabyte SDSS dataset. More importantly, we attain the computational efficiency needed to process the next generation of surveys—surveys that will include  $\mathcal{O}(100)$  petabytes of image data.

6.1. *Hardware.* Our test platform was the Cori supercomputer—a machine currently ranked eighth in the global “Top 500” rankings ([Top500.org 2017](#)). Cori comprises 9,688 compute nodes connected by a high-speed network ([NERSC 2018](#)). Each compute node has 112 GB of memory and one processor, an Intel Xeon Phi 7250, commonly referred to as “Knights Landing.” Knights Landing runs at 1.4 GHz: every second 1.4 billion clock cycles elapse. Knights Landing more than makes up for this relatively slow clock by executing many instructions in parallel during each clock cycle. A single Knights Landing processor has 68 cores—physically distinct regions of the processor that execute instructions in parallel. Each core simultaneously runs two hardware threads that appear to the operating system as separate cores. A hardware thread executes batches of instructions twice per clock cycle: once on the “up-tick” and once on the “down-tick.” During each tick, a hardware thread may execute the same instruction on eight different 64-byte floating point numbers. This is known as single-instruction multiple-data (SIMD) parallelism. In addition to supporting common instructions, like “add” and “multiply,” Knights Landing also has a “fused multiply-add” (FMA) instruction that adds two numbers and then multiplies their sum by a third, all during one tick of a clock cycle. FMAs can effectively double the throughput for programs that have a suitable pattern of addition and multiplication.

6.2. *Efficient thread-level execution.* Supercomputer programs are written almost exclusively in verbose languages like assembly, Fortran, C, and C++. Many statisticians, however, prefer high-productivity languages like R and Python. These languages often require a  $5\times$  to  $10\times$  fewer lines of code to express the same algorithm. Unfortunately, these languages often run  $10\times$ ,  $100\times$ , or even  $1000\times$  slower than equivalent C code ([Julia developers 2018](#)), making them inadmissible for high-performance computing.

Our work uses the Julia programming language ([Bezanson et al. 2017](#)) for the first time in an HPC setting. Julia matches both the succinctness of scripting languages and the speed of C. The “hot spots” in a Julia codebase, however, must be written carefully to attain C-like speed. The process

of converting Julia code to run in an HPC setting is iterative. It begins with profiling a typical program execution to find the hot spots: intuition is a poor substitute for measurement. The first round of bottlenecks often involve memory allocation, where the program requests that the operating system assign it more memory. We removed all these memory allocations from loops that contribute significantly to runtime by allocating the memory up front. After removing memory allocations, our next round of bottlenecks was due to memory access; processors cannot execute instructions until data has been transferred from main memory to the processor’s registers. A hardware thread could remain idle for approximately 200 clock cycles while fetching one number from main memory. Memory-access bottlenecks need to be fixed on a case-by-case basis. The solution typically involves some reordering of the computation to enable better prefetching of data from main memory. In some cases, we save time by recomputing values rather than fetching them.

6.3. *Multi-node scaling.* In HPC, a program’s scalability is how its performance varies with the capacity of the hardware devoted to executing the program (Hager & Wellein 2010). We assess scaling empirically in two ways. First, we vary the number of compute nodes while keeping the amount of work constant per compute node (“weak scaling”); many compute nodes solve a much larger problem. Here the problem size is the area of the sky that we are constructing a catalog for. Second, we vary the number of compute nodes while keeping the total job size constant (“strong scaling”); many compute nodes have to further subdivide the problem. The two scaling metrics give different perspectives to inform predictions about how a particular supercomputer program will perform on future datasets, which may be much larger than any used for testing.

Generally, it is harder to use more compute nodes efficiently. Ideal weak scaling is constant runtime as the number of compute nodes increases. Figure 17a shows, instead, runtime roughly doubling as the number of compute nodes increases from 1 to 8192. Ideal strong scaling is runtime that drops by a factor of  $1/c$  when the number of compute nodes grows by a factor of  $c$ . Figure 17b shows, instead, runtime roughly halving as the number of compute nodes quadruples from 2048 to 8192.

Additionally, the scaling graphs break out runtime by component. The *image loading* component is time taken to load images while worker threads are idle. After the first task, images are prefetched in the background, so the majority of image loading time accrues up front. Image loading time is constant in the weak scaling graph and proportional to the number of nodes in the strong scaling graph—exactly what we want. We are not disk or bandwidth

limited, even at high node counts.

The *load imbalance* component is time when processes are idle because no tasks remain, but the job has not ended because at least one process has not finished its current task. Both scaling graphs indicate that load imbalance is our primary scaling bottleneck. Fortunately, load imbalance is due to having only 4 tasks per process. With at least  $1000\times$  more data, as we expect from LSST, the load imbalance should become negligible.

The *task processing* component is the main work loop. It involves no network or disk I/O: only computation and shared memory access. Because of that, task processing serves as a sanity check for both graphs: it should, and does, stay roughly constant in the weak scaling graph and vary in proportion to the number of nodes in the strong scaling graph.

The *other* component is everything else. It is always a small fraction of the total runtime. It includes scheduling overhead, all network I/O (excluding image loading), and writing output to disk.

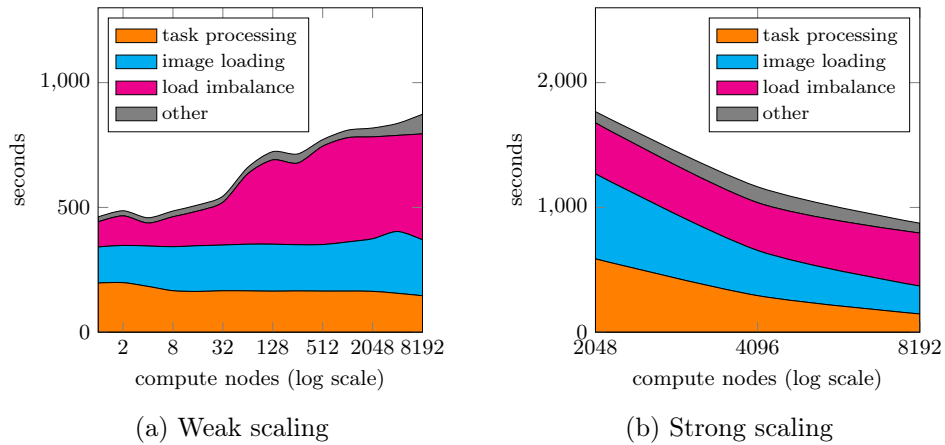


Fig 17: Scaling results. See accompanying discussion of load imbalance.

6.4. *Peak performance.* To assess the peak performance that can be accomplished for Bayesian inference at scale, we prepared a specialized configuration for performance measurement in which the processes synchronize after loading images, prior to task processing. We ran this configuration on 9568 Cori Intel Xeon Phi nodes, each running 17 processes of eight threads each, for a total of 1,303,832 threads. 57.8 TB of image data was processed over a ten-minute interval. The peak performance achieved was 1.54 PFLOP/s. This is the first time a supercomputer program in any language besides C, C++, Fortran, and assembly has exceeded one petaflop.



**7. Discussion.** We presented Bayesian inference for constructing an astronomical catalog based on a scientifically accurate model. We approximated the posterior for a large image dataset and demonstrated the scaling characteristics necessary to apply Bayesian inference to hundreds of petabytes of images from the next generation of astronomical surveys. Our optimization procedure found a stationary point, even though doing so required treating the full dataset as a single optimization problem. We conclude that even for large datasets, it is not necessary to resort to heuristics when Bayesian inference is preferable, or to settle for recovering just the mode of the posterior.

Both our inference procedures—MCMC and VI—compared favorably to the current standard practice for constructing catalogs, reducing error across the board, and reducing error for colors by up to half. Also, in contrast to current standard practice, both inference procedures quantify uncertainty based on a realistic model of the data. On synthetic data, MCMC was better at quantifying uncertainty, likely due to the restrictive form of the variational distribution. Additionally, MCMC provided uncertainty estimate for all latent random variables, whereas VI modeled some random variables as point masses—in effect recovering maximum a posteriori (MAP) estimates for them. However, MCMC was approximately  $1000\times$  slower than VI.

On real data, while both inference procedures’ point estimates were better than current standard practice, neither procedures’ uncertainty estimates were well calibrated. Uncalibrated uncertainties can nonetheless be useful, e.g., for flagging particularly unreliable point estimates. Additionally, even if the uncertainties are ignored by downstream analyses, point estimates are typically better if ambiguity is modeled.

Uncertainty quantification may be particularly susceptible to model misspecification. For questions requiring calibrated uncertainties, enhancing the galaxy model may help by reducing model misspecification. Though the galaxy model we use—one with elliptical contours—is standard in astronomy, a more flexible galaxy model shows promise (Regier et al. 2015).

Neither MCMC nor VI could be applied to our model without customization. The need for problem-specific adjustments is a barrier to the broader adoption of both techniques. For MCMC, for example, we went through several iterations before settling on slice sampling and AIS. VI required even more problem-specific customization. Our VI techniques include: 1) approximating an integrand with its second order Taylor expansion; 2) approximating the point spread function with a mixture of Gaussians; 3) upper bounding the KL divergence between the color and a GMM prior; 4) limiting the variational distribution to a structured mean-field form; 5) limiting

the variational distribution to point masses for some parameters; and 6) optimizing the variational lower bound with a variant of Newton's method rather than coordinate ascent. This final technique was particularly laborious, as it involved manually deriving and implementing both gradients and Hessians for a complicated function.

Because of the relative ease of deriving and implementing MCMC, it could be a useful tool for trying different models and testing for misspecification before implementing VI. In some cases, it may be simpler to expend more computational resources to scale up the MCMC procedure than to implement VI. For the most computationally intensive problems, however, only VI is practical at present. For these problems, VI is a good alternative both to MAP estimation and to heuristic algorithms.

## APPENDIX A: KULLBACK-LEIBLER DIVERGENCES

This section gives the formulas for common Kullback-Leibler divergences that appear in the derivation of variational lower bound.

The KL divergence for  $a_s$  is between two categorical distributions.

$$(44) \quad D_{\text{KL}}(q(a_s), p(a_s)) = \acute{a}_s \log \frac{\acute{a}_s}{\mathcal{A}} + (1 - \acute{a}_s) \log \frac{1 - \acute{a}_s}{1 - \mathcal{A}}$$

The KL divergence for  $u_s$  is between a point mass and a uniform distribution.

$$(45) \quad D_{\text{KL}}(q(u_s), p(u_s)) = \frac{1}{360 \times 180}$$

The KL divergence for  $e_s^{\text{angle}}$  is between a point mass and a uniform distribution.

$$(46) \quad D_{\text{KL}}(q(e_s^{\text{angle}}), p(e_s^{\text{angle}})) = \frac{1}{180}$$

The KL divergence for  $e_s^{\text{radius}}$  is between a point mass and a log-normal distribution.

$$(47) \quad D_{\text{KL}}(q(e_s^{\text{radius}}), p(e_s^{\text{radius}})) = -\log 2\pi - \frac{1}{2} \log \mathcal{E}_2^{\text{radius}} - \frac{(\acute{e}_s^{\text{radius}} - \mathcal{E}_1^{\text{radius}})^2}{2\mathcal{E}_2^{\text{radius}}}$$

The KL divergence for  $e_s^{\text{profile}}$  is between a point mass and a Beta distribution. Here B denotes the beta function.

$$(48) \quad D_{\text{KL}}(q(e_s^{\text{profile}}), p(e_s^{\text{profile}})) = (\mathcal{E}_1^{\text{profile}} - 1) \log \acute{e}_s^{\text{profile}} + (\mathcal{E}_2^{\text{profile}} - 1) \log(1 - \acute{e}_s^{\text{profile}}) - \text{B}(\mathcal{E}_1^{\text{profile}}, \mathcal{E}_2^{\text{profile}})$$

The KL divergence for  $e_s^{\text{axis}}$  is between a point mass and a Beta distribution.

$$(49) \quad D_{\text{KL}}(q(e_s^{\text{axis}}), p(e_s^{\text{axis}})) = (\mathcal{E}_1^{\text{axis}} - 1) \log \acute{e}_s^{\text{axis}} + (\mathcal{E}_2^{\text{axis}} - 1) \log(1 - \acute{e}_s^{\text{axis}}) - \text{B}(\mathcal{E}_1^{\text{axis}}, \mathcal{E}_2^{\text{axis}})$$

The KL divergence for  $r_s^{\text{axis}}$  is between two log-normal distributions.

$$(50) \quad D_{\text{KL}}(q(r_s | a_s = i), p(r_s | a_s = i)) = \log \frac{\mathcal{R}_{i2}}{\hat{r}_{si}} + \frac{\hat{r}_{si} + (\acute{r}_{si} - \mathcal{R}_{i1})^2}{2\mathcal{R}_{i2}} - \frac{1}{2}$$

## REFERENCES

- Bertin, E. & Arnouts, S. (1996), ‘SExtractor: Software for source extraction’, *Astronomy and Astrophysics Supplement Series* **117**(2), 393–404.
- Bezanson, J., Edelman, A., Karpinski, S. & Shah, V. B. (2017), ‘Julia: A fresh approach to numerical computing’, *SIAM Review* **59**(1), 65–98.
- Bickel, P. J. & Doksum, K. A. (2015), *Mathematical Statistics: Basic Ideas and Selected Topics*, Vol. 1, 2 edn, CRC Press, chapter 5, pp. 306–307.
- Bishop, C. M. (2006), *Pattern Recognition and Machine Learning*, Springer.
- Blei, D. M., Kucukelbir, A. & McAuliffe, J. D. (2017), ‘Variational inference: A review for statisticians’, *Journal of the American Statistical Association* .
- Brewer, B. J., Foreman-Mackey, D. & Hogg, D. W. (2013), ‘Probabilistic catalogs for crowded stellar fields’, *The Astronomical Journal* **146**(1), 7.
- Doi, M., Tanaka, M. et al. (2010), ‘Photometric response functions of the Sloan Digital Sky Survey imager’, *The Astronomical Journal* **139**(4).
- Fan, Y. & Sisson, S. A. (2011), ‘Reversible jump markov chain monte carlo’, *Handbook of Markov Chain Monte Carlo* pp. 67–92.
- Feroz, F., Hobson, M. P. & Bridges, M. (2009), ‘MultiNest: An efficient and robust Bayesian inference tool for cosmology and particle physics’, *Monthly Notices of the Royal Astronomical Society* **398**(4), 1601–1614.
- Gelman, A., Carlin, J. B., Stern, H. S., Dunson, D. B., Vehtari, A. & Rubin, D. B. (2014), Basics of markov chain simulation, in ‘Bayesian data analysis’, Vol. 3, CRC Press, chapter 11.
- Gelman, A. & Rubin, D. B. (1992), ‘Inference from iterative simulation using multiple sequences’, *Statistical science* pp. 457–472.
- Green, P. J. (1995), ‘Reversible jump Markov chain Monte Carlo computation and Bayesian model determination’, *Biometrika* **82**(4), 711–732.
- Greisen, E. W. & Calabretta, M. R. (2002), ‘Representations of world coordinates in FITS’, *Astronomy & Astrophysics* **395**(3), 1061–1075.
- Hager, G. & Wellein, G. (2010), *Introduction to High Performance Computing for Scientists and Engineers*, CRC Press.
- Hershey, J. R. & Olsen, P. A. (2007), Approximating the Kullback Leibler divergence between Gaussian mixture models, in ‘IEEE International Conference on Acoustics, Speech and Signal Processing’.
- Julia developers (2018), ‘Julia micro-benchmarks’, <https://julialang.org/benchmarks/>. [Online; accessed January 23, 2018].
- Lang, D. & Hogg, D. (2015), ‘Tractor: Astronomical source detection, separation, and photometry’, <http://thetractor.org/>. [Online; accessed January 30, 2015].
- Loredo, T. J. (2013), Bayesian astrostatistics: A backward look to the future, in ‘Astrostatistical Challenges for the New Astronomy’, Springer, pp. 15–40.
- LSST (2017), ‘About LSST’, <http://www.lsst.org/about>. [Online; accessed September 12, 2017].
- Lupton, R., Gunn, J. et al. (2001), ‘The SDSS imaging pipelines’, *arXiv preprint astro-ph/0101420* .
- Lupton, R. H., Ivezić, Z. et al. (2005), SDSS image processing II: The photo pipelines, Technical report, Princeton University.
- Mandel, K. S., Narayan, G. & Kirshner, R. P. (2011), ‘Type Ia supernova light curve inference: Hierarchical models in the optical and near-infrared’, *The Astrophysical Journal* **731**(2), 120.
- Murphy, K. P. (2012), *Machine Learning: A Probabilistic Perspective*, MIT Press.

- Neal, R. M. (2001), ‘Annealed importance sampling’, *Statistics and Computing* **11**(2), 125–139.
- Neal, R. M. (2003), ‘Slice sampling’, *Annals of Statistics* pp. 705–741.
- NERSC (2018), ‘Cori configuration’, <http://www.nersc.gov/users/computational-systems/cori/configuration/>. [Online; accessed January 23, 2018].
- Nocedal, J. & Wright, S. (1999), ‘Numerical optimization’, *Springer Science* **35**, 67–68.
- Portillo, S. K. N., Lee, B. C. G., Daylan, T. & Finkbeiner, D. P. (2017), ‘Improved point source detection in crowded fields using probabilistic cataloging’, *arXiv preprint arXiv:1703.01303*.
- Regier, J., McAuliffe, J. & Prabhat (2015), ‘A deep generative model for astronomical images of galaxies’, *NIPS Workshop: Advances in Approximate Bayesian Inference*.
- SDSS (2017), ‘Measures of flux and magnitude’, <http://www.sdss3.org/dr8/algorithms/magnitudes.php>. [Online; accessed November 12, 2017].
- SDSS (2018a), ‘Camera’, <http://www.sdss.org/instruments/camera/>. [Online; accessed January 30, 2018].
- SDSS (2018b), ‘Sky coverage’, <http://classic.sdss.org/dr7/coverage/>. [Online; accessed January 30, 2018].
- Top500.org (2017), ‘Top500 list – November 2017’, <http://www.top500.org/list/2017/11/>. [Online; accessed November 16, 2017].
- von Hippel, T., Jefferys, W. H. et al. (2006), ‘Inverting color-magnitude diagrams to access precise star cluster parameters: A Bayesian approach’, *The Astrophysical Journal* **645**(2), 1436.

JEFFREY REGIER  
 DEPARTMENT OF ELECTRICAL ENGINEERING  
 AND COMPUTER SCIENCES  
 UNIVERSITY OF CALIFORNIA, BERKELEY  
 465 SODA HALL  
 BERKELEY, CA 94720  
 USA  
 E-MAIL: [jregier@eecs.berkeley.edu](mailto:jregier@eecs.berkeley.edu)

ANDREW C. MILLER  
 SCHOOL OF ENGINEERING  
 AND APPLIED SCIENCES  
 HARVARD UNIVERSITY  
 29 OXFORD STREET  
 CAMBRIDGE, MA 02138  
 USA  
 E-MAIL: [acm@seas.harvard.edu](mailto:acm@seas.harvard.edu)

DAVID SCHLEGEL  
 LAWRENCE BERKELEY NATIONAL LABORATORY  
 1 CYCLOTRON ROAD  
 BERKELEY, CA 94720  
 USA  
 E-MAIL: [djschlegel@lbl.gov](mailto:djschlegel@lbl.gov)

RYAN P. ADAMS  
 PRINCETON UNIVERSITY  
 DEPARTMENT OF COMPUTER SCIENCE  
 35 OLDEN STREET  
 PRINCETON, NJ 08540  
 USA  
 E-MAIL: [rpa@princeton.edu](mailto:rpa@princeton.edu)

JON D. MCAULIFFE  
 DEPARTMENT OF STATISTICS  
 UNIVERSITY OF CALIFORNIA, BERKELEY  
 367 EVANS HALL  
 BERKELEY, CA 94720  
 USA  
 E-MAIL: [jon@stat.berkeley.edu](mailto:jon@stat.berkeley.edu)

PRABHAT  
 LAWRENCE BERKELEY NATIONAL LABORATORY  
 1 CYCLOTRON ROAD  
 BERKELEY, CA 94720  
 USA  
 E-MAIL: [prabhat@lbl.gov](mailto:prabhat@lbl.gov)